Journal of Alloys and Compounds 928 (2022) 167185

Contents lists available at ScienceDirect

Journal of Alloys and Compounds

journal homepage: www.elsevier.com/locate/jalcom

Manganese and oxygen dual-doping MoS_2 boosts reduction and adsorption activity toward efficient recovery of gold(I) from thiosulfate solutions

Yumeng Liang[a,1], Weiquan Zhan[a,b,*,1], Yuan Yuan[a,b], Noe Zamora-Romero[b], Feifei Jia[a,**], Bingqiao Yang[c], Zamoniddin Nasrddinov[d], José Luis Arauz-Lara[b], Shaoxian Song[a]

[a] Hubei Key Laboratory of Mineral Resources Processing and Environment, Wuhan University of Technology, Luoshi Road 122, Wuhan, Hubei 430070, China
[b] Instituto de Fisica, Universidad Autonoma de San Luis Potosi, Av. Manuel Nava 6, Zona Universitaria, C.P. 78290 San Luis Potosi, SLP, Mexico
[c] School of Xingfa Mining Engineering, Wuhan Institute of Technology, Xiongchu Avenue 693, Wuhan, Hubei 430073, China
[d] Mining-metallurgical Institute of Tajikistan, Navruz St., Baston Tajik, Tajikistan

ARTICLE INFO

Article history:
Received 2 January 2022
Received in revised form 5 September 2022
Accepted 12 September 2022
Available online 14 September 2022

Keywords:
Photocatalytic reduction
Gold(I)
Mn and O co-doping
MoS_2

ABSTRACT

The necessity for application of molybdenum disulfide (MoS_2) in photocatalytic reduction field required speedy improvement with high reduction and adsorption performance. Here, manganese (Mn) and oxygen (O) dual-doping strategy were taken for demonstrating that enhancing photocatalytic reduction could achieve simultaneous modulation of the reduction and adsorption parameters by optimizing the electronic configuration and hydrophilicity ability in MoS_2. Benefiting from the Mn and O dual-doping collective effect, the developed Mn,O-MoS_2 exhibited outstanding photocatalytic reduction and recovery performances of gold(I) from thiosulfate leaching solutions with reduction capacity of 1386.98 mg/g and the corresponding recovery of 92.50%. Besides, Mn and O atoms dual doping in MoS_2 accelerated the recovery rate, which was 3 folds higher compared with that of MoS_2. Experimental and first-principle approaches suggested that the reduction and adsorption ability of MoS_2 were strengthened through tuning the electronic structure and surface property with Mn and O dopants: (1) Mn atoms notably enhanced the conductivity and optimized the electronic structure for facilitating the reduction performance; (2) The incorporated O atoms greatly promoted the adsorption of $[Au(S_2O_3)_2]^{3-}$ by improving the affinity of water molecules and Mn,O-MoS_2. The work provides a promising strategy to manipulate two-dimensional materials for various applications about catalysts and adsorbent.

1. Introduction

MoS_2, a typical earth-abundant transition metal dichalcogenides (TMDs), had emerged as a strong candidate for photocatalytic reduction of heavy metal ions [1] such as chromium(VI) [2], silver(I) [3] and gold(I) [4] with the aim of removal or recovery because of their favorable photocatalytic properties. Take photocatalytic reduction of gold(I) for example, a new method to extract gold from thiosulfate leaching solutions. Thiosulfate leaching [5] was the most potential technique to replace cyanidation leaching [6] for leaching gold from natural ores, alluvial deposits or urban mines[7] through conversing gold into a water-soluble coordination compound ($[Au(S_2O_3)_2]^{3-}$) [8]. However, the recovery of gold(I) from thiosulfate leaching solutions was current a bottleneck problem for its industrial application.

Even though tremendous techniques including cementation [9], metal displacement [10], adsorption [11] and ion-exchange [12] had been applied for recycling gold(I) from thiosulfate leaching solutions, the cost or recovery was still unsatisfied. Lately, photocatalytic reduction of $[Au(S_2O_3)_2]^{3-}$ by MoS_2 was an efficient method for recycling gold(I), and simultaneously simplifying the traditional recovery steps [13]. Although the recovery of $[Au(S_2O_3)_2]^{3-}$ was improved using MoS_2 compared with traditional materials, the performances were yet unsatisfactory. The photocatalytic reduction

* Corresponding author at: Hubei Key Laboratory of Mineral Resources Processing and Environment, Wuhan University of Technology, Luoshi Road 122, Wuhan, Hubei 430070, China.
** Corresponding author.
E-mail addresses: zhan_weiquan@163.com (W. Zhan), feifeijia@whut.edu.cn (F. Jia).
[1] Co-first author.

https://doi.org/10.1016/j.jallcom.2022.167185
0925-8388/

performances were related with reduction and adsorption activity. Lots of previous researches had verified that the conductivity of MoS_2 was low, limiting the transfer of photo-generated electrons [14–16]. In addition, the surface of MoS_2 was hydrophobic, which was not available for the hydrated gold(I) bound with sulfur atoms.

An alternative approach to solving the above problems was through tuning the electronic and surface structure of MoS_2, such as, by heteroatoms doping [17–19], thus improving the ability of photocatalytic reduction. Transition metal doping engineering had been regarded as a promising method to regulate the electronic structure. In previous studies, metal-doped catalysts, for example, Co-doped [20], Ni-doped [21], Mn-doped [22], Zn-doped MoS_2 [23], had outstanding reduction activity. While the metal doping was effective in inducing active site and optimizing the electronic structure for reduction, their adsorption toward hydrated ions was poor due to the hydrophobic property of MoS_2. Anion doping, especially hydrophilic oxygen doping, had been reported that could modulate the affinity between MoS_2 with water molecules [24]. Besides, Xie and coworker [25] found that the incorporation of oxygen into MoS_2 with numerous defects could increase the active sites. Whereas, it was still a question whether the structure engineering by atoms doping technique could simultaneously influence the reduction and adsorption factors for photocatalytic reduction ability.

Herein, the structural engineering of MoS_2 by Mn and O doping through a facile one-pot hydrothermal method was successfully achieved and systematically studied in this work. Mn and O dopants as regulatory factors were adopted to optimize the electronic status and surface property of MoS_2 for achieving highly active catalytic centers being most favorable to the photocatalytic reduction of $[Au(S_2O_3)_2]^{3-}$. The photocatalytic reduction behaviors of $[Au(S_2O_3)_2]^{3-}$ on Mn and O codoped MoS_2 (Mn,O-MoS_2) was studied in aqueous solutions. The aim was to understand the photocatalytic reduction behaviors of $[Au(S_2O_3)_2]^{3-}$ on Mn,O-MoS_2, thus to pave a new way for the recovery of precious metal through photocatalytic reduction.

2. Experimental section

2.1. Materials

Chloroauric acid ($HAuCl_4$, 1000 ppm) was purchased from Well Group Scientific Ltd. (USA). Ammonium thiosulfate ($H_8N_2O_3S_2$) was obtained from Aladdin Co. (Shanghai, China). Other reagents used in the experiment were all purchased from Sinopharm Chemical Reagent Co., Ltd. (China). The water used in all the experiments was produced by Millipore Super Q system with a resistivity of 18.2 MΩ·cm.

2.2. Materials Synthesis

Mn,O-MoS_2 was synthesized through one-step hydrothermal reaction. Typically, 1 mmol ammonium molybdate tetrahydrate ($(NH_4)_6Mo_7O_{24}.4\ H_2O$), 30 mmol thiourea ($CN_2H_4S$) and 0.05 mmol manganese chloride ($MnCl_2.4\ H_2O$) were dissolved into 32 mL of water under magnetic stirring for 1 h. Followed on, the solution was transferred into a 50 mL Teflon-lined stainless-steel autoclave and kept in an oven at 180 °C for 24 h. After naturally cooled down to room temperature, the resultant precipitates were collected by filtration, washed with water and ethanol several times, and finally dried at 60 °C in vacuum oven. For comparison, O-MoS_2 was prepared following similar synthesized route with the absence of $MnCl_20.4\ H_2O$. Mn-MoS_2 was synthesized by the same procedure but heated through hydrothermal reaction at 220 °C. MoS_2 was yielded under hydrothermal reaction at 220 °C without $MnCl_20.4\ H_2O$. According to the chemical component analysis through inductively coupled plasma-optical emission spectrometry (ICP-OES), the component of obtained MoS_2, Mn-MoS_2, O-MoS_2 and Mn,O-MoS_2 sample is $Mo_{0.5002}S$, $Mo0._{4911}Mn_{0.004}S$, $Mo_{0.5218}O_{0.4146}S$ and $Mo_{0.5213}Mn_{0.005}O_{0.2946}S$, respectively.

2.3. Reduction experiments

Initial $[Au(S_2O_3)_2]^{3-}$ solution (150 mL, 100 mg·L^{-1}) was prepared by dropwise adding $HAuCl_4$ (15 mL) in $H_8N_2O_3S_2$ (45 mg) under pH of 10, as reported in previous work [22]. Subsequently, samples (10 mg) were added into $[Au(S_2O_3)_2]^{3-}$ solution under the natural light with the intensity of about 0.04 KW/m^2. At various time intervals (0–1200 min), 1 mL reaction suspension was sucked and then filtered. In the experiment about pH effect on $[Au(S_2O_3)_2]^{3-}$ solution, $[Au(S_2O_3)_2]^{3-}$ solutions with pH ranging from 8 to 12 were taken on. For investigating the initial $[Au(S_2O_3)_2]^{3-}$ concentration on reduction, $[Au(S_2O_3)_2]^{3-}$ solutions with various initial concentration (50, 75, 100, 125 and 150 mg·L^{-1}) were performed.

The Au (I) reduction was calculated as the following equation:

$$R = \frac{C_0V_0 - CV}{m} \quad (1)$$

The recovery rate in the first 120 min was calculated by the following equation:

$$\text{Recovery rate}(mg{\cdot}g^{-1}{\cdot}min^{-1}) = \frac{R}{t} \quad (2)$$

And the recovery in 1200 min was calculated using the following equation:

$$\text{Recovery}(\%) = \frac{C_0 - C}{C_0} \times 100\% \quad (3)$$

where R was the Au (I) reduction on sample, mg/g; C_0 and C exhibited $[Au(S_2O_3)_2]^{3-}$ reduction before and after reduction, respectively, mg·L^{-1}; V_0 and V were volume of solution before and after reduction, respectively, L; m meant the mass of sample, g; t was the time, min.

2.4. DFT calculations

All the DFT calculations were carried out using DMol3 program. The plane wave cutoff energy was 340 eV, and k-point calculation in the Brillouin zone was set to 5x5x1. Lattice geometries and atomic positions were totally relaxed until the atomic force doesn't exceed 0.002 Hartree/Å, and the convergence threshold for energy was 10^{-6} eV. The non-local exchange and correlation effects was described used the Perdew-Bruker-Ernzerh functional within the Generalized Gradient Approximation (GGA), which is an auxiliary proof of interaction between Au and Mn,O-MoS_2 [26]. Spin-polarized density functional theory is employed in the electronic structure calculations. In all calculations, the vacuum layer was set as 20 Å for eliminating periodic interaction. Mn-MoS_2 was built through substituting one Mo atom with Mn atom. To account for different O dopant concentrations, a single dopant and two dopants in Mn-MoS_2 supercell were considered. All the possible configurations of Mn,O-MoS_2 were exhibited in Fig. S1. Before the explorations in the interaction among H_2O, Au(I) and catalysts, the stability of Mn,O-MoS_2 was evaluated by the formation energies (E_{form}) showed below:

$$E_{form} = E_{doped} - E_{pure} + n(\mu_{Mo} - \mu_{Mn}) + m(\mu_S - \mu_O) \quad (4)$$

where E_{doped} and E_{pure} were the total energy of Mn,O-MoS_2 and MoS_2, respectively; μ_{Mo}, μ_{Mn}, μ_S and μ_O were the chemical potentials of Mo, Mn, S and O, respectively. n and m meant the numbers of removed Mo and S atoms, respectively. μ_{Mo} and μ_S are the total energy per atom of the bcc Mo and orthorhombic α-S, respectively. μ_O is the single O atom in the total energy of O_2 molecule. According to the definition, the formation energies were calculated as exhibited in Table S1. The formation energy of MoS_2-Mn-1 $O_{(1)}$ and MoS_2-Mn-2 $O_{(1)}$ was the

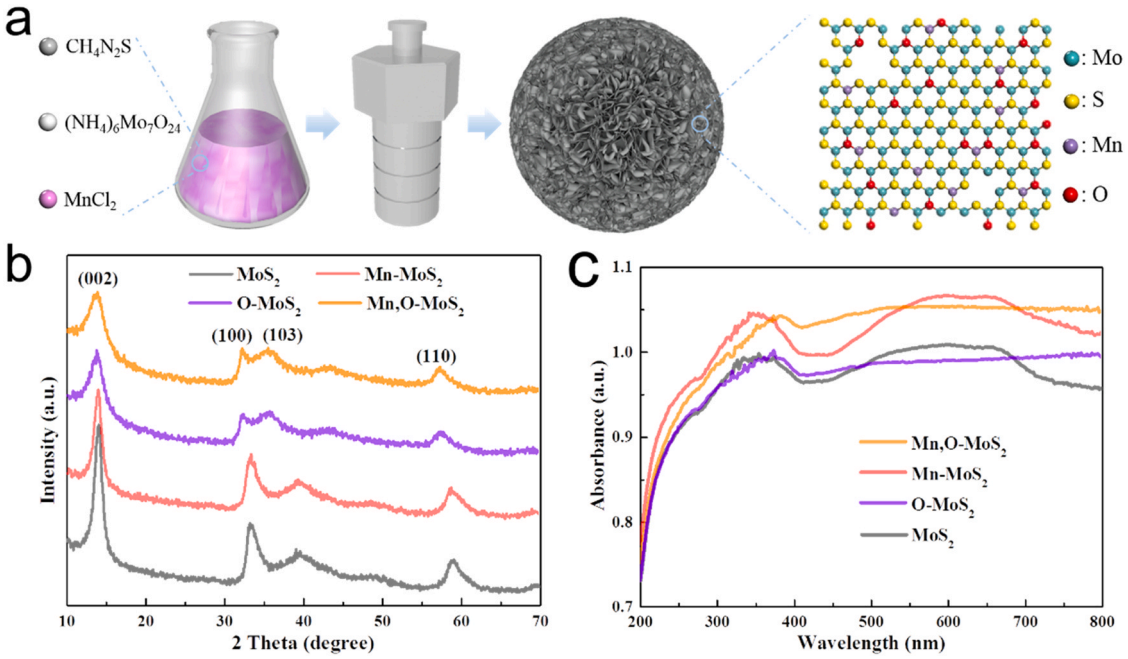

Fig. 1. a) Schematic illustration of the synthetic approach for Mn,O-MoS_2; b) XRD patterns and c) UV-Vis absorbance spectra of MoS_2, O-MoS_2, Mn-MoS_2 and Mn,O-MoS_2.

highest in the single O dopant and two O dopants in Mn-MoS_2 models, respectively, demonstrating that the stable structure and O atoms preferred to connect with Mn atoms. In addition, in the electron density maps of Mn,O-MoS_2 after structure optimization (Fig. S2), Mn and O atoms could well incorporate into the structure of MoS_2. In the following experiment, MoS_2-Mn-1 $O_{(1)}$ and MoS_2-Mn-2 $O_{(1)}$ were used for investigating O dopant on the structure and Au(I) adsorption on Mn,O-MoS_2. The adsorption energy between Au(I) and catalysts was calculated as below:

$$\Delta E_{catalyst/Au(I)} = E_{catalyst/Au(I)} - E_{catalyst} - E_{Au(I)} \quad (5)$$

$$\Delta E_{catalyst/H_2O} = (E_{catalyst/H_2o} - E_{catalyst} - nE_{H_2O})/n \quad (6)$$

$$\Delta E_{Au(I)/H_2O} = (E_{Au(I)/H_2o} - E_{Au(I)} - nE_{H_2O})/n \quad (7)$$

where *catalyst* meant MoS_2, Mn-MoS_2, O-MoS_2 or Mn,O-MoS_2, $\Delta E_{catalyst/Au(I)}$ was the adsorption energies between catalyst and Au(I), $\Delta E_{catalyst/H_2O}$ and $\Delta E_{Au(I)/H_2O}$ represented the interaction energy between H_2O and catalyst (or Au(I)), n was the number of H_2O molecules in the system, $E_{catalyst/Au(I)}$, $E_{catalyst}$, $E_{Au(I)}$, $E_{catalyst/H_2o}$, E_{H_2O} and $E_{Au(I)/H_2o}$ were the energy of catalyst-Au(I) system, catalyst system, an isolated Au(I) system, catalyst-H_2O system, H_2O system and Au(I)-H_2O system in a vacuum box, respectively.

2.5. Materials characterizations

The phase structures of all samples were identified by a D8 Advance system with Cu-Kα radiation (Bruker AXS, Germany). XPS was recorded on a Thermo ESDALB 250 Xi spectrometer. The Zeta potential was measured by a Malvern Zeta-sizer Nano ZS90 (UK). The contact angle is determined by a goniometer (JC2000DM). Chemical component analysis of samples was detected with ICP-OES (Leeman Prodigy 7, America). Photoluminescence spectrum were performed on excitation with a wavelength of about 325 nm using a Xe lamp as the excitation source (Edinburgh FLS1000, UK). Surface morphology was detected by scanning electron microscope (SEM) (Phenom ProX G6, Netherlands). The morphologies and microstructures of samples and corresponding energy dispersive spectra (EDS) were observed by a JEM-2100 F transmission electron microscope. Atomic structure was directly observed using Titan Cubed Themis G2 300 (Thermo Fisher Scientific, America). UV-Vis was performed on a Lambda 750 S UV-Vis spectrophotometer (America). An Agilent 200 series AA atomic adsorption spectrophotometer (AAS) was used for detecting the concentration of Au(I).

2.6. Electrochemical measurements

All the electrochemical measurements were conducted in a three electrode system with 0.5 M H_2SO_4 as electrolyte using an electrochemical station (CHI1030B, China). For preparation of the working electrodes, 10 mg sample was dispersed in 1 mL of ethanol. Saturated calomel electrode, Pt flake and ITO glass deposited with samples were used as reference electrode, counter electrode and working electrode, respectively. Photocurrent measurements were carried out under xenon lamp with 300 W light intensity, and the interval of light on/off was set to 30 s. Electrochemical impedance spectroscopy (EIS) analysis was attained in a 1 M potassium ferricyanide solution with an alternating current voltage of 10 mN over the frequency range of 0.01–10^5 Hz. Mott-Schottky (M-S) analysis was performed with the test frequency of 1000 Hz.

3. Results and discussion

3.1. Morphology and structure analysis

A facile hydrothermal reaction was applied for fabricating Mn,O-MoS_2 (more details in the Experimental Section), as depicted in Fig. 1a. In the strategy of hydrothermal doping, ammonium molybdate tetrahydrate, thiourea and manganese chloride were used as Mo, S and Mn source, respectively, while the introduction of O resource was through adjusting the hydrothermal temperature. Phase structures were detected by X-ray diffraction (XRD), as shown in Fig. 1b. The diffraction peaks of all prepared samples could be indexed into the crystalline planes of MoS_2 phase[27]. No other peaks appeared, confirming that the structure of MoS_2 hadn't been affected as incorporating Mn and O atoms. When oxygen atoms were incorporated into MoS_2, all the peaks were broadened and the (103) diffraction peaks of MoS_2 shifted to a lower angle, resulting from the declined crystallinity in accordance with previous work[28].

According to the diffraction theory, the diffraction peaks will be broadened by the declined crystal structure and the crystal defects. After Mn atoms doping, the width of all diffraction peaks broadened owing to the created defects by the dopant[28]. When O oxygen atoms were introduced, the reduced crystallinity broadened all the diffraction peaks[25]. And the (103) diffraction peaks of MoS_2 shifted to a lower angle, resulting from the declined crystallinity. It was indicated that the synthesized temperature played an important role in the formation crystal structure. The analyses reveal that insufficient reaction leads to the incorporation of O atoms[29]. Contact angle of MoS_2, Mn-MoS_2, O-MoS_2 and Mn,O-MoS_2 was tested as shown in Fig. S3. The hydrophilcity of MoS_2 and Mn-MoS_2 was poor, but that was dramatically improved after O atoms doping like O-MoS_2 and Mn,O-MoS_2. Ultraviolet-visible absorption (UV-Vis) measurements were applied for measuring the optical properties of MoS_2, O-MoS_2, Mn-MoS_2 and Mn,O-MoS_2, as showed in Fig. 1c. All the samples had a broad adsorption in the visible light and ultraviolet (UV) region. It was worth noticing that Mn,O-MoS_2 possessed highest adsorption intensity among the prepared samples, thus Mn,O-MoS_2 was likely to be a superior visible light and UV responsive photocatalyst.

To get insights into the morphology and microstructure of Mn,O-MoS_2, SEM, transmission electron microscope (TEM) and aberration-corrected scanning transmission electron microscope (STEM) measurements were carried out. As Fig. S4 implied, all the samples (MoS_2, O-MoS_2, Mn-MoS_2 and Mn,O-MoS_2) exhibited similar flower-like morphology, indicating that incorporated Mn and O atoms wouldn't affect the morphology. In the TEM images (Fig. 2a), it could be seen that Mn,O-MoS_2 showed ultrathin nanosheet morphology and obvious ripples. No particles were observed, which excluded the possibility of other impurity formation. The high-resolution TEM (HRTEM) image of Mn,O-MoS_2 (Fig. 2b) revealed an interplanar spacing of 0.63 nm, which could be assigned to the (002) crystal facet of MoS_2. Large crystal defects (as marked by the cycles) were observed, benefiting the photocatalytic reduction of $[Au(S_2O_3)_2]^{3-}$ [30]. The structure of Mn,O-MoS_2 was further verified by its selected area electron diffraction (SAED) tests (Fig. 2c). Additionally, corresponding EDS elemental mapping images (Fig. 2d) manifested the presence of Mo, S, Mn and O elements in Mn,O-MoS_2. The homogenous distribution of Mn and O elements demonstrated their co-doping into MoS_2 nanosheets.

Furthermore, the atomic structure and Mn substitutional doping were directly observed in the high-angle annular dark-field STEM (HAADF-STEM) image (Fig. 2e). Honeycomb lattice clearly visualized meant the structure model of 2 H-MoS_2, as indicated by the rectangle. 1 T phase MoS_2 could be observed as displayed in Fig. S5. The higher the atomic number, the brighter the reaction appears on the image[31]. Because of the difference in atomic number in Mn and Mo atoms, Mn atoms marked by a white dotted circle were doped at Mo sites, exhibiting single atom substitutional doping[32]. It should be noted that some lattice disorder regions could be detected, resulting from the existence of defects, which well matched the existence state of S elemental measured by XPS (Fig. 3b). The existence of defects may strengthen the interaction between MoS_2 and Au[33]. Taken together, these atomic resolution STEM images directly prove that Mn atoms have been incorporated in the MoS_2 lattice.

Apart from the above techniques, X-ray photoelectron spectroscopy (XPS) was performed as well to further probe the surface-chemical states of component elements in Mn,O-MoS_2. The spin-orbit Mo^{IV} $3d_{3/2}$, Mo^{IV} $3d_{5/2}$ and S 2 s orbitals of Mo and S modes were observed at 232.58, 230.48 and 226.28 eV, respectively (Fig. 3a), and this matched well with 2 H-MoS_2 phase [34]. The peak at 235.78 eV in Mo 3d spectra could be ascribed to high-oxidation-state Mo in the Mo 3d spectra (Mo^{6+}), which was consistent with the previous results [35,36]. Particularly, the deconvolution of Mo 3d peaks displayed the components at 232.38 and 229.18 eV that belonged to the 1 T-MoS_2 phase in accord with previous work [37,38]. Normally, metallic 1 T-MoS_2 benefited the enhancement of photocatalytic ability, compared with 2 H-MoS_2. In Fig. 3b, it was obvious that the S 2p region implied doublet peaks at 163.38 and 162.18 eV, belonging to the typical binding energy of S 2p1/2 and S 2p3/2, respectively [39]. Meanwhile, an additional peak at 164.68 eV could be identified as the edge S in line with related literature [37]. At the same time, the presence of O 1 s signal at 530.18 eV provided solid evidence for O doping in Mn,O-MoS_2 (Fig. 3c)[40]. What's more, Mn 2p signal was detected at 641.08 eV (Fig. 3d), confirming the doping of Mn in Mn,O-MoS_2 [41]. The results revealed that the successful co-doping of Mn and O atoms in the structure of Mn,O-MoS_2.

3.2. Recovery performances

To evaluate the performances of Mn,O-MoS_2 as an efficient photocatalyst for photocatalytic reducing $[Au(S_2O_3)_2]^{3-}$, a series of measurements were carried out. The photocatalytic reduction performances of $[Au(S_2O_3)_2]^{3-}$ on MoS_2, O-MoS_2, Mn-MoS_2 and Mn,O-MoS_2 as function of time were tested under natural light irradiation, and the results were showed in Fig. 4a. The reduction of $[Au(S_2O_3)_2]^{3-}$ boosted at first and then balanced at around 500 min. It was clear that the incorporation of single atoms e.g. O or Mn atoms in MoS_2 would benefit the reduction of $[Au(S_2O_3)_2]^{3-}$. Mn and O co-doping into MoS_2 dramatically enhance the reduction ability with high reduction capacity of 1386.98 mg/g, which was 2.5 times than MoS_2. Besides, Mn and O atoms dual doping in MoS_2 accelerate the recovery rate, which was 3 folds higher compared with that of MoS_2 (Fig. 4b). Remarkably, about 95% recovery was achieved for $[Au(S_2O_3)_2]^{3-}$ solutions in 1200 min using Mn,O-MoS_2, while the recovery by MoS_2 was only 37.84% (Fig. 4c). For further studying about the reduction reaction, the reduction experiment was carried out in dark environment, as shown in Fig. S7. The reduction capacity of $[Au(S_2O_3)_2]^{3-}$ in sunlight irradiation was about 2.26 times than that in dark condition. The result revealed that the reduction reaction in dark condition might be consisted of adsorption and chemical reduction [13], but catalytic reduction was in the dominant position. In Fig. 4d, the reduction capacity of $[Au(S_2O_3)_2]^{3-}$ on Mn,O-MoS_2 increased with the increase of initial concentration, demonstrating that Mn,O-MoS_2 could be well applied for recovering $[Au(S_2O_3)_2]^{3-}$. pH was considered as an impact factor for investigating the reduction performance of $[Au(S_2O_3)_2]^{3-}$ on Mn,O-MoS_2, as displayed in Fig. 4e. The reduction of $[Au(S_2O_3)_2]^{3-}$ increased quickly firstly and then slowly as pH increasing. More importantly, zeta potential exhibited the same results, the negative potential fast and then slowly (Fig. 4f). Thus, it could be concluded that interaction between H^+ and unsaturated S atom decreased, exposing more active sites on Mn,O-MoS_2 for interacting with $[Au(S_2O_3)_2]^{3-}$ when pH increased.

After being applied as catalyst for reducing and recovering $[Au(S_2O_3)_2]^{3-}$, Mn,O-MoS_2 was explored using XRD, XPS and TEM. XRD pattern of crystal structure about Mn,O-MoS_2 after reduction was depicted in Fig. 5a. Four diffraction peaks at 38.19°, 44.39°, 64.66° and 77.58° were assigned to the crystal plane of Au^0 [42]. The characteristic peaks of Mn,O-MoS_2 were not observed after reducing $[Au(S_2O_3)_2]^{3-}$ might owing to its quite small proportion. Wide-scan XPS spectrum of Mn,O-MoS_2 after reducing $[Au(S_2O_3)_2]^{3-}$ was exhibited in Fig. S6a, and Au^0 could be found. The Mo 3d, Mn 2p, O 1 s and S 2p spectra in Fig. S6b-e, and revealed that no new peaks and changes occurred on Mo, Mn, O and S, which demonstrated no chemical reaction happened. The Au $4f_{5/2}$ and Au $4f_{7/2}$ peaks at 87.40 and 83.75 eV in Fig. 5b were assigned to Au^0, further demonstrating the reduction of $[Au(S_2O_3)_2]^{3-}$ into gold nanoparticles. Lots of gold nanoparticles could be obviously observed in Fig. 5c. In the HRTEM images (Fig. 5d), it was found that Au^0 interacted closely with Mn,O-MoS_2, and the structure of Mn,O-MoS_2 was not affected.

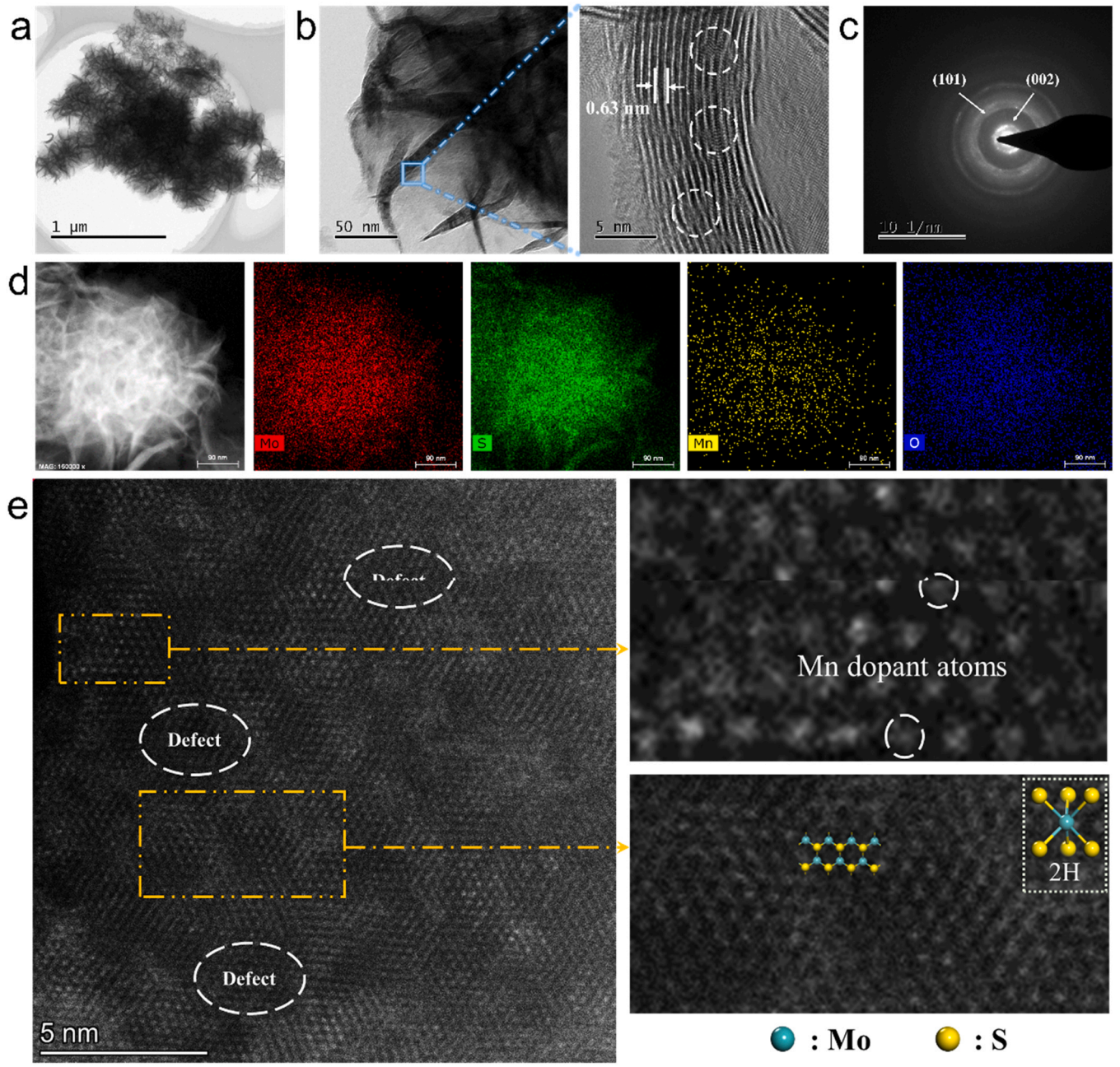

Fig. 2. Morphological and structural characterizations. a) TEM, b) HRTEM, c) SAED, d) corresponding EDS elemental mapping, and e) HAADF-STEM images of M,O-MoS_2.

From Fig. 5e, the corresponding EDS elemental mappings indicated that Mo, S, Mn and O owned same distribution area, and Au was evenly distributed on nanoparticles, further exhibiting the reduction of $[Au(S_2O_3)_2]^{3-}$ into Au^0.

3.3. Catalytic reduction mechanism

To explore mechanism of the enhancement in recycling $[Au(S_2O_3)_2]^{3-}$ using Mn,O-MoS_2, the electronic structure properties and adsorption behaviors were researched. Transient photocurrent response and EIS were applied to investigate the transfer efficiency of photo-generated charges. In Fig. 6a, incorporating Mn or O atoms in MoS_2 would increase photocurrent intensity, indicating the quicker transfer of photo-electrons. Also, the photocurrent response of Mn-MoS_2 was higher than O-MoS_2. Mn,O-MoS_2 exhibited greatest photocurrent intensity among the prepared samples, illustrating the beneficiation of Mn and O co-doping in photocatalytic performance. Photoluminescence emission spectroscopy was used to explore the charge transfer as emissions result from recombination of charge carriers associated with energy gap[43,44]. In the Fig. S8, Mn,O-MoS_2 owned the lowest emission in the samples, which resulted from slow recombination of photo-generated electrons and holes, thus improving the photo catalytic activity. EIS tests revealed the smallest semicircle of Mn,O-MoS_2 in the prepared samples, which indicated the lowest charge-transfer resistance (Fig. 6b). Further, the charge-transfer resistance of Mn-MoS_2 was smaller than O-MoS_2. Based on the above discussions, Mn-MoS_2 was more conductive to catalytic reduction than O-MoS_2. However, the reduction capacity of $[Au(S_2O_3)_2]^{3-}$ on O-MoS_2 was higher than that of Mn-MoS_2, which might originate from the enhanced adsorption ability. The efficient reduction of $[Au(S_2O_3)_2]^{3-}$ on Mn,O-MoS_2 could be ascribed to the super transfer photoelectrons and low charge-transfer resistance.

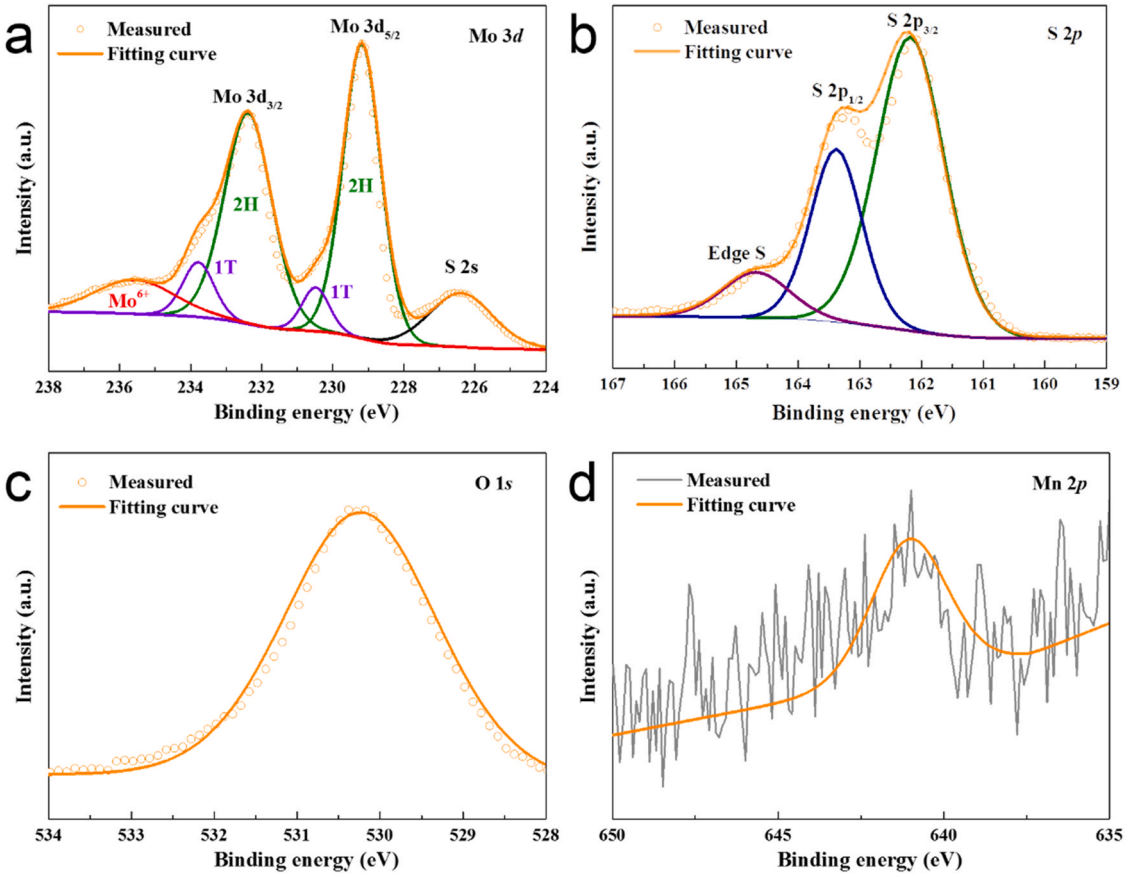

Fig. 3. a) Mo 3d XPS spectrum, b) S 2p XPS spectrum, c) O 1 s XPS spectrum, and d) Mn 2p XPS spectrum of Mn,O-MoS_2.

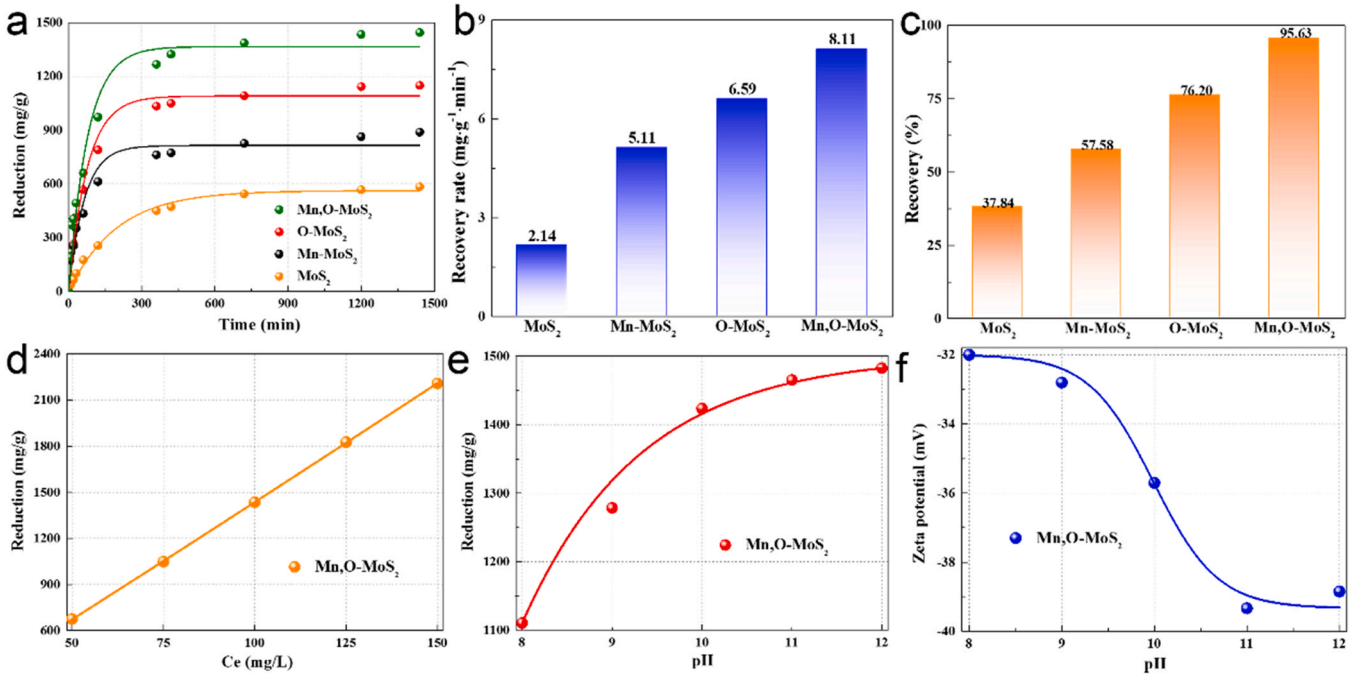

Fig. 4. Photocatalytic reduction performances. a) Reduction as a function of reaction time; b) Recovery rate in the first 120 min; c) Recovery in 1200 min; d) Effect of initial gold concentration on reduction performance; e) Effect of pH on reduction performance; f) Zeta potential of Mn,O-MoS_2.

With the aim of studying the reduction mechanism in detail, the Kubelka-Munk transformed reference spectra (Fig. 6c) and Mott-Schottky plot (Fig. 6d) of Mn,O-MoS_2 were obtained to investigate the band structure and conduction band, respectively. The band energy of Mn,O-MoS_2 was calculated as blow equation [45]:

$$(\alpha hv)^n = A(hv - E_g) \quad (8)$$

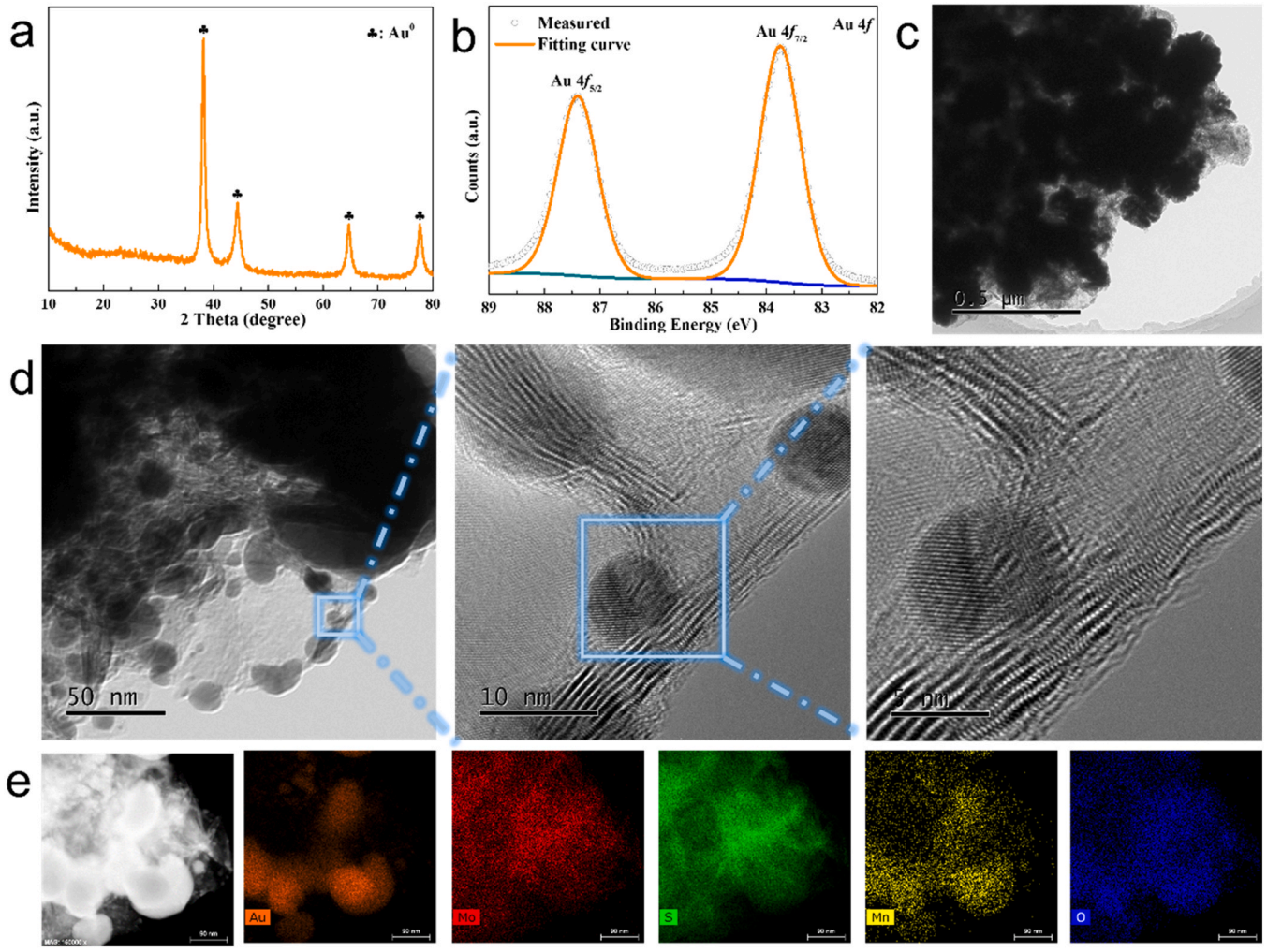

Fig. 5. Structure and morphology characterization of Mn,O-MoS_2 after reduction. a) XRD pattern; b) Au 4 f XPS spectrum; c) TEM image, d) HRTEM images, e) corresponding EDS elemental mappings.

where α, h, v, *A* and E_g represented absorption coefficient, Planck's constant, light frequency, a constant and band gap, respectively, the index $n = 2$ was used in the work. The bandgap (E_g) of Mn,O-MoS_2 was estimated as 1.48 eV, which expressed the quick generation of photo-electrons that attributed to the introduction of Mn and O atoms. Furthermore, the flat-band potential (E_{fb}) of Mn,O-MoS_2 was found to be at − 0.42 V in the Mott-Schottky result. The slop of the curve was positive, indicating the n-type characteristic of Mn,O-MoS_2. As n-type semiconductor, E_{fb} was close to conduction band. Therefore, the conduction band value of Mn,O-MoS_2 was roughly

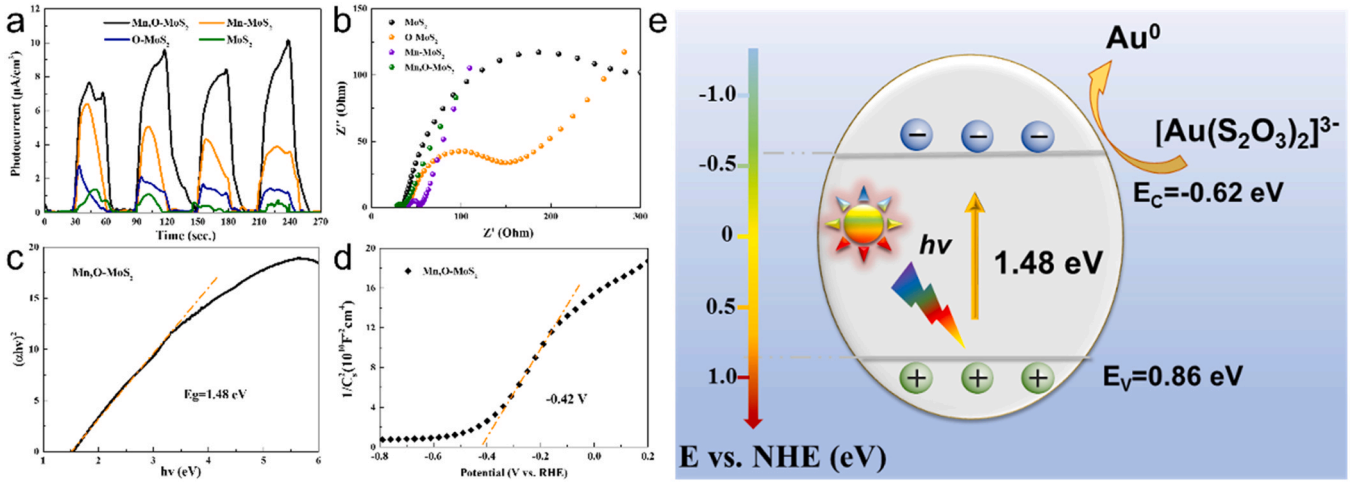

Fig. 6. a) Photocurrent responses, b) EIS results of MoS_2, O-MoS_2, Mn-MoS_2 and Mn,O-MoS_2; c) Kubelka-Munk transformed reference spectrum, d) and Mott-Schottky plot of Mn,O-MoS_2; e) schematic illustrating the band structure and relevant redox potential.

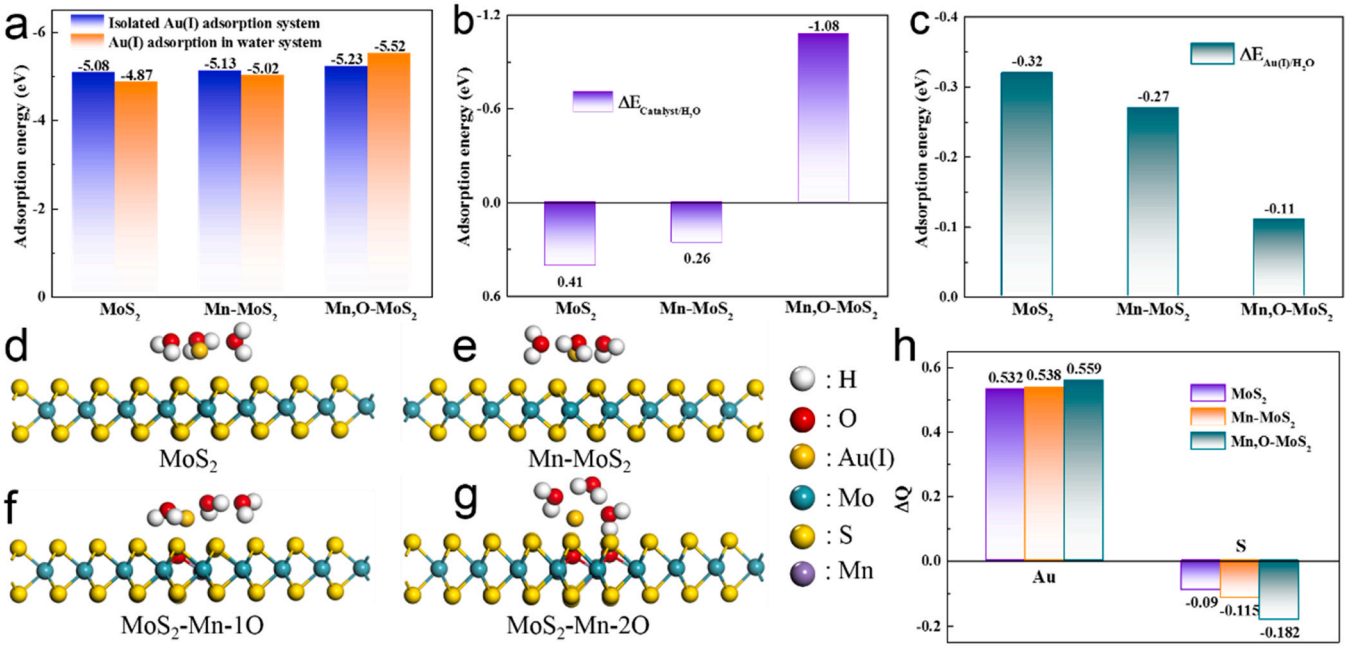

Fig. 7. a) Interaction energy between Au(I) and catalysts in isolated and water system; b) Interaction energy between H_2O and catalysts in the water system; c) Interaction energy between Au(I) and H_2O in water system; d-g) side views of configuration with Au(I) and H_2O on the surface of MoS_2, Mn-MoS_2 and Mn,O-MoS_2; h) Milliken atomic charge changes of Au(I) and S atoms.

calculated to be about − 0.62 eV. And the valance band (VB) edge was calculated according to following formula:

$$E_V = E_g + E_C \quad (9)$$

According to the equation, the valance band edge of Mn,O-MoS_2 was around 0.86 eV. The schematic illustration of redox potential and the band structure of Mn,O-MoS_2 were exhibited in Fig. 6e. Under visible light irradiation, photo-generated electrons-holes pairs were produced. The conduction band of Mn,O-MoS_2 was more negative than the reduction potential of $[Au(S_2O_3)_2]^{3-}/Au^0$ (0.15 eV), demonstrating that $[Au(S_2O_3)_2]^{3-}$ could be photocatalytic reduced into Au^0 on Mn,O-MoS_2.

DFT calculations were then carried out for fundamentally understanding the enhanced photocatalytic reduction performances of the Mn and O co-doped MoS_2. Conductivity and intrinsic activity were considered to be the important impacts on improving the photocatalytic reduction activity. Pristine MoS_2 had a bandgap of 1.82 eV (Fig. S9a), which was in line with previous results [46]. The value of bandgap became narrower to 0.95 eV after displacing one Mo atom by a Mn atom (Fig. S9b), revealing that the transfer of photo-electrons enhanced. When one O atom was incorporated into the structure of Mn-MoS_2, the bandgap presented a slight decrease of 0.03 eV (Fig. S9c). In addition, the density of state (DOS) was calculated and showed in Fig. S9d-f. It was clear that doping Mn and O atoms affected the band structure near the Fermi level. Reduced bandgaps of doped MoS_2 might effectively contribute to the improvement in conductivity thus to enhance the photocatalytic activity. Compared with Mn atoms, the incorporation of O atoms had little influence on the catalytic performances.

It was well-known that adsorption was another key factor to directly determine the photocatalytic reduction ability, so the interaction between Au(I) and catalysts was calculated. Adsorption energies between Au(I) and catalysts in isolated and water system were given in Fig. 7a. Whether in isolated or water system, the adsorption energy of Au(I) on MoS_2 was enhanced as incorporating Mn or O atoms. Doping O atoms could better strengthen the adsorption of Au(I) on MoS_2 than incorporating Mn atoms, exhibiting that O atoms possessed strong affinity to Au(I). The phenomenon could be ascribed to the stronger electronegativity of oxygen atoms. Accounting for the effects of water, the adsorption energies of Au(I) on MoS_2 and Mn-MoS_2 decreased compared with that in isolated system, but opposite in Au(I) adsorption on the surface of Mn,O-MoS_2. To understand the observations better, interaction energies between H_2O and catalysts (Fig. 7b) and interaction energies between H_2O and Au(I) (Fig. 7c) were studied. In adsorption of Au(I) on pure MoS_2 system, H_2O strongly interacted with Au(I) but less with MoS_2, revealing the hydration of Au(I) and the hydrophobicity of MoS_2 (Fig. 7d). After doping Mn atoms, the interaction between H_2O and MoS_2 slightly enhanced, resulting in the decreased interaction between Au(I) and H_2O (Fig. 7e). When O atoms were doped into Mn-MoS_2, the affinity between H_2O and MoS_2 was greatly improved, which might originate from the hydrogen-bond interaction between H atoms (H_2O molecules) and O atoms (Mn,O-MoS_2). Meanwhile, the interaction between Au(I) and H_2O weakened, leading to the destruction of hydration of Au(I) (Fig. 7f-g). As a consequence, the absorbed H_2O would drag Au(I) close to the surface of Mn,O-MoS_2, thereby dramatically facilitating the adsorption of Au(I) on Mn,O-MoS_2.

To further clarify the interaction between Au(I) and Mn,O-MoS_2, electron density maps, partial density of states (PDOS) and Milliken atomic charges were calculated. In Fig. S10, the electron cloud between Au(I) and O atoms overlap (in both H_2O and Mn,O-MoS_2), indicating strong affinity of Au(I) to H_2O and also to Mn,O-MoS_2. For studying the interaction mechanism among Au(I), H_2O and Mn,O-MoS_2, PDOS of the interaction among Au(I), O (oxygen atoms in Mn,O-MoS_2) and H (hydrogen atoms in H_2O molecules) was given in Fig. S11. It was obvious that Au *d* orbitals strongly bonded with O *s* orbitals in the range of − 10–0 eV, exhibiting the interaction between Au and O atoms on the surface of Mn,O-MoS_2. There existed sparse overlap between H orbitals and O orbitals, which meant that the interaction between H_2O molecules and Mn,O-MoS_2 might be due to hydrogen bonding. Milliken atomic charge changes (ΔQ) of Au(I) and S atoms were investigated before and after interaction between Au(I) and the catalysts in the presence of water (Fig. 7h). It was found that Au(I) was positively charged after adsorption but opposite in S atoms, demonstrating the interaction between Au(I) and S atoms.

After incorporating Mn atoms, the charges of Au(I) slightly increased but remarkably improved when Mn and O atoms were both doped into MoS_2, which demonstrated the strong interaction between Au(I) and Mn,O-MoS_2. Also, the charges change of S atoms had the same tendency with that of Au(I), which exhibited that the incorporation of O atoms could facilitate the interaction between Au(I) and S atoms. As a result, Mn,O-MoS_2 had a strong adsorption of Au(I), benefiting the photocatalytic reduction of $[Au(S_2O_3)_2]^{3-}$.

4. Conclusion

In summary, Mn,O-MoS_2 nanosheets were successfully synthesized using a simple one-pot hydrothermal method. The structure of MoS_2 had been tuned to achieve favorable properties for photocatalytic reduction of $[Au(S_2O_3)_2]^{3-}$. Specifically, the reduction capacity of $[Au(S_2O_3)_2]^{3-}$ by Mn,O-MoS_2 were 1386.98 mg/g, and the corresponding recovery was 92.50%. Mn and O dopants optimized the electronic status and surface property of MoS_2 for achieving highly adsorption and catalytic reaction, thus to be most favorable to photocatalytic reduction of $[Au(S_2O_3)_2]^{3-}$. This work could be potentially extended to other transition metal dichalcogenides, aiming at gaining desired strategies for various applications.

CRediT authorship contribution statement

Yumeng Liang: Writing – original draft, Software. **Weiquan Zhan:** Supervision, Investigation, Data curation, Modification. **Yuan Yuan:** Formal analysis. **NOE Zamora-Romero:** Equipment support. **Feifei Jia:** Data curation, Validation. **Bingqiao Yang:** Conceptualization. **Zamoniddin:** Equipment support. **José Luis Arauz-Lara:** Validation. Shaoxian Song: Conceptualization.

Data Availability

No data was used for the research described in the article.

Declaration of Competing Interest

The authors declare that they have no known competing financial interests or personal relationships that could have appeared to influence the work reported in this paper.

Acknowledgements

The work is financially supported by the National Key Research and Development Program of China (2021YFC2900900). Zhan gratefully acknowledges the Consejo Nacional de Ciencia y Tecnología (CONACYT) of Mexico for offering him the scholarship under the grant No. 813934 during his Ph.D. studies.

Appendix A. Supporting information

Supplementary data associated with this article can be found in the online version at doi:10.1016/j.jallcom.2022.167185.

References

[1] Y. Chen, M. Xu, J. Wen, Y. Wan, Q. Zhao, X. Cao, Y. Ding, Z.L. Wang, H. Li, Z. Bian, Selective recovery of precious metals through photocatalysis, Nat. Sustain. 4 (2021) 618–626, https://doi.org/10.1038/s41893-021-00697-4

[2] W. Zou, Z. Liu, R. Li, C. Jin, X. Zhang, K. Jiang, Photoinduced transformation of silver ion by molybdenum disulfide nanoflakes at environmentally relevant concentrations attenuates its toxicity to freshwater algae, J. Hazard. Mater. 416 (2021) 126043, https://doi.org/10.1016/j.jhazmat.2021.126043

[3] Z. Wang, B. Mi, Environmental applications of 2D molybdenum disulfide (MoS_2) nanosheets, Environ. Sci. Technol. 51 (2017) 1–42, https://doi.org/10.1021/acs.est.7b01466

[4] W. Zhan, Y. Yuan, B. Yang, F. Jia, S. Song, Construction of MoS_2 nano-heterojunction via ZnS doping for enhancing in-situ photocatalytic reduction of gold thiosulfate complex, Chem. Eng. J. 394 (2020) 124866, https://doi.org/10.1016/j.cej.2020.124866

[5] R. Wang, C. Zhang, Y. Zhao, Y. Zhou, E. Ma, J. Bai, J. Wang, Recycling gold from printed circuit boards gold-plated layer of waste mobile phones in “mild aqua regia” system, J. Clean. Prod. 278 (2021) 123597, https://doi.org/10.1016/j.jclepro.2020.123597

[6] A.W. Schuppe, G.M. Borrajo-Calleja, S.L. Buchwald, Enantioselective olefin hydrocyanation without cyanide, J. Am. Chem. Soc. 141 (2019) 18668–18672, https://doi.org/10.1021/jacs.9b10875

[7] X. Zeng, J.A. Mathews, J. Li, Urban mining of E-waste is becoming more cost-effective than virgin mining, Environ. Sci. Technol. 52 (2018) 4835–4841, https://doi.org/10.1021/acs.est.7b04909

[8] D.T. Sun, N. Gasilova, S. Yang, E. Oveisi, W.L. Queen, Rapid, Selective Extraction of Trace Amounts of Gold from Complex Water Mixtures with a Metal-Organic Framework (MOF)/Polymer Composite, J. Am. Chem. Soc. 140 (2018) 16697–16703, https://doi.org/10.1021/jacs.8b09555

[9] M. Karavasteva, Kinetics and deposit morphology of gold cemented on magnesium, aluminum, zinc, iron and copper from ammonium thiosulfate-ammonia solutions, Hydrometallurgy 104 (2010) 119–122, https://doi.org/10.1016/j.hydromet.2010.04.007

[10] B. Xu, K. Li, Q. Li, Y. Yang, X. Liu, T. Jiang, Kinetic studies of gold leaching from a gold concentrate calcine by thiosulfate with cobalt-ammonia catalysis and gold recovery by resin adsorption from its pregnant solution, Sep. Purif. Technol. 213 (2019) 368–377, https://doi.org/10.1016/j.seppur.2018.12.064

[11] S. Chen, F. Zi, X. Hu, Y. Chen, P. Yang, Q. Wang, X. Qin, H. Cheng, Y. Liu, Y. He, C. Wang, D. Hu, Y. Liu, Y. Zhang, Interfacial properties of mercaptopropyl-functionalised silica gel and its adsorption performance in the recovery of gold(I) thiosulfate complex, Chem. Eng. J. 393 (2020) 124547, https://doi.org/10.1016/j.cej.2020.124547

[12] M. Laatikainen, T. Sainio, Ion exchange in complexing media-Nickel removal from ammoniacal ammonium sulfate solutions, Chem. Eng. J. 373 (2019) 831–839, https://doi.org/10.1016/j.cej.2019.05.128

[13] P. Chen, Y. Liang, B. Yang, F. Jia, S. Song, In situ reduction of Au(I) for efficient recovery of gold from thiosulfate solution by the 3D MoS_2/chitosan aerogel, ACS Sustain. Chem. Eng. 8 (2020) 3673–3680, https://doi.org/10.1021/acssuschemeng.9b06639

[14] M. Ahmadi, O. Zabihi, R. Yadav, M.R.G. Ferdowsi, M. Naebe, The reinforcing role of 2D graphene analogue MoS_2 nanosheets in multiscale carbon fibre composites: improvement of interfacial adhesion, Compos. Sci. Technol. 207 (2021) 108717, https://doi.org/10.1016/j.compscitech.2021.108717

[15] L.H. Hu, P.C. Chen, Hot-injection for synthesizing ammonium thiosulfate precursor of molybdenum disulfide thin film coated on nano-porous aluminum oxide for surface strengthening, J. Alloy. Compd. 848 (2020) 156262, https://doi.org/10.1016/j.jallcom.2020.156262

[16] F. Jia, C. Liu, B. Yang, S. Song, Microscale control of edge defect and oxidation on molybdenum disulfide through thermal treatment in air and nitrogen atmospheres, Appl. Surf. Sci. 462 (2018) 471–479, https://doi.org/10.1016/j.apsusc.2018.08.166

[17] S. Bolar, S. Shit, J.S. Kumar, N.C. Murmu, R.S. Ganesh, H. Inokawa, T. Kuila, Optimization of active surface area of flower like MoS_2 using V-doping towards enhanced hydrogen evolution reaction in acidic and basic medium, Appl. Catal. B Environ. 254 (2019) 432–442, https://doi.org/10.1016/j.apcatb.2019.04.028

[18] J. Pető, T. Ollár, P. Vancsó, Z.I. Popov, G.Z. Magda, G. Dobrik, C. Hwang, P.B. Sorokin, L. Tapasztó, Spontaneous doping of the basal plane of MoS_2 single layers through oxygen substitution under ambient conditions, Nat. Chem. 10 (2018) 1246–1251, https://doi.org/10.1038/s41557-018-0136-2

[19] W. Xiao, P. Liu, J. Zhang, W. Song, Y.P. Feng, D. Gao, J. Ding, Dual-Functional N Dopants in Edges and Basal Plane of MoS_2 Nanosheets Toward Efficient and Durable Hydrogen Evolution, Adv. Energy Mater. 7 (2017) 1–10, https://doi.org/10.1002/aenm.201602086

[20] D.C. Nguyen, T.L. Luyen Doan, S. Prabhakaran, D.T. Tran, D.H. Kim, J.H. Lee, N.H. Kim, Hierarchical Co and Nb dual-doped MoS_2 nanosheets shelled micro-TiO_2 hollow spheres as effective multifunctional electrocatalysts for HER, OER, and ORR, Nano Energy 82 (2021) 105750, https://doi.org/10.1016/j.nanoen.2021.105750

[21] Y. Xue, X. Bai, Y. Xu, Q. Yan, M. Zhu, K. Zhu, K. Ye, J. Yan, D. Cao, G. Wang, Vertically oriented Ni-doped MoS_2 nanosheets supported on hollow carbon microtubes for enhanced hydrogen evolution reaction and water splitting, Compos. Part B Eng. 224 (2021) 109229, https://doi.org/10.1016/j.compositesb.2021.109229

[22] W. Zhan, Y. Yuan, X. Yao, B. Yang, F. Jia, C. Lin, J.L. Arauz-Lara, S. Song, Efficient recovery of Gold(I) from thiosulfate solutions through photocatalytic reduction with Mn(II)-doped MoS_2, ACS Sustain. Chem. Eng. 9 (2021) 11681–11690, https://doi.org/10.1021/acssuschemeng.1c02160

[23] Y. Yao, H. Hu, H. Zheng, F. Wei, M. Gao, Y. Zhang, S. Wang, Zn-MoS_2 nanocatalysts anchored in porous membrane for accelerated catalytic conversion of water contaminants, Chem. Eng. J. 398 (2020) 125455, https://doi.org/10.1016/j.cej.2020.125455

[24] W. Zhan, F. Jia, Y. Yuan, C. Liu, K. Sun, B. Yang, Controllable incorporation of oxygen in MoS_2 for efficient adsorption of Hg^{2+} in aqueous solutions, J. Hazard. Mater. 384 (2020) 1–10, https://doi.org/10.1016/j.jhazmat.2019.121382

[25] J. Xie, J. Zhang, S. Li, F. Grote, X. Zhang, H. Zhang, R. Wang, Y. Lei, B. Pan, Y. Xie, Controllable disorder engineering in oxygen-incorporated MoS_2 ultrathin

nanosheets for efficient hydrogen evolution, J. Am. Chem. Soc. 135 (2013) 17881–17888, https://doi.org/10.1021/ja408329q
[26] P. Akhtar, M.J.I. Khan, Z. Kanwal, S.M. Ramay, A. Mahmood, M. Saleem, Ab-initio and experimental investigations on Au incorporated MoS_2 for electronic and optical response, J. Alloy. Compd. 877 (2021) 160244, https://doi.org/10.1016/j.jallcom.2021.160244
[27] Y. Yuan, B. Yang, F. Jia, S. Song, Reduction mechanism of Au metal ions into Au nanoparticles on molybdenum disulfide, Nanoscale 11 (2019) 9488–9497, https://doi.org/10.1039/c8nr09420a
[28] J. Liu, Z. Wang, J. Li, L. Cao, Z. Lu, D. Zhu, Structure engineering of MoS_2 via simultaneous oxygen and phosphorus incorporation for improved hydrogen evolution, Small 16 (2020) 1–11, https://doi.org/10.1002/smll.201905738
[29] T. Sun, Z. Li, X. Liu, L. Ma, J. Wang, Oxygen-incorporated MoS_2 microspheres with tunable interiors as novel electrode materials for supercapacitors, J. Power Sources 352 (2017) 135–142, https://doi.org/10.1016/j.jpowsour.2017.03.123
[30] D. Gupta, V. Chauhan, R. Kumar, A comprehensive review on synthesis and applications of molybdenum disulfide (MoS_2) material: past and recent developments, Inorg. Chem. Commun. 121 (2020) 108200, https://doi.org/10.1016/j.inoche.2020.108200
[31] G. Bai, S. Yuan, Y. Zhao, Z. Yang, S.Y. Choi, Y. Chai, S.F. Yu, S.P. Lau, J. Hao, 2D layered materials of rare-earth Er-doped MoS_2 with NIR-to-NIR down- and up-conversion photoluminescence, Adv. Mater. 28 (2016) 7472–7477, https://doi.org/10.1002/adma.201601833
[32] W. Zhan, Y. Yuan, C. Liu, P. Chen, Y. Liang, Y. Wang, J.L. Arauz-Lara, F. Jia, Preparation and application of 0D, 2D and 3D molybdenite: a review, Miner. Miner. Mater. 1 (2022) 5, https://doi.org/10.20517/mmm.2022.04
[33] Z. Li, D. Zhou, J. Xiangke, Highly selective adsorption on monolayer MoS_2 doped with Pt, Ag, Au and Pd and effect of strain engineering: a DFT study, Sens. Actuators, A Phys. 322 (2021), https://doi.org/10.1016/j.sna.2021.112637
[34] K. Ai, C. Ruan, M. Shen, L. Lu, MoS_2 nanosheets with widened interlayer spacing for high-efficiency removal of mercury in aquatic systems, Adv. Funct. Mater. 26 (2016) 5542–5549, https://doi.org/10.1002/adfm.201601338
[35] T. Sun, J. Wang, X. Chi, Y. Lin, Z. Chen, X. Ling, C. Qiu, Y. Xu, L. Song, W. Chen, C. Su, Engineering the electronic structure of MoS_2 nanorods by N and Mn dopants for ultra-efficient hydrogen production, ACS Catal. 8 (2018) 7585–7592, https://doi.org/10.1021/acscatal.8b00783
[36] D. Wang, X. Zhang, S. Bao, Z. Zhang, H. Fei, Z. Wu, Phase engineering of a multiphasic 1T/2H MoS_2 catalyst for highly efficient hydrogen evolution, J. Mater. Chem. A 5 (2017) 2681–2688, https://doi.org/10.1039/c6ta09409k
[37] W.Y. Zhou, S.S. Li, X.Y. Xiao, S.H. Chen, J.H. Liu, X.J. Huang, Defect- and phase-engineering of Mn-mediated MoS_2 nanosheets for ultrahigh electrochemical sensing of heavy metal ions: chemical interaction-driven in situ catalytic redox reactions, Chem. Commun. 54 (2018) 9329–9332, https://doi.org/10.1039/c8cc04575e
[38] J. Li, A. Listwan, J. Liang, F. Shi, K. Li, J. Jia, High proportion of 1 T phase MoS_2 prepared by a simple solvothermal method for high-efficiency electrocatalytic hydrogen evolution, Chem. Eng. J. 422 (2021) 130100, https://doi.org/10.1016/j.cej.2021.130100
[39] Z. Zheng, S. Cong, W. Gong, J. Xuan, G. Li, W. Lu, F. Geng, Z. Zhao, Semiconductor SERS enhancement enabled by oxygen incorporation, Nat. Commun. 8 (2017) 2–11, https://doi.org/10.1038/s41467-017-02166-z
[40] V.H. Hoa, D.T. Tran, D.C. Nguyen, D.H. Kim, N.H. Kim, J.H. Lee, Molybdenum and phosphorous dual doping in cobalt monolayer interfacial assembled cobalt nanowires for efficient overall water splitting, Adv. Funct. Mater. 2002533 (2020) 1–12, https://doi.org/10.1002/adfm.202002533
[41] H. Tan, C. Wang, W. Hu, H. Duan, P. Guo, N. Li, G. Li, L. Cai, Z. Sun, F. Hu, W. Yan, Reversible tuning of the ferromagnetic behavior in Mn-doped MoS_2 nanosheets via interface charge transfer, ACS Appl. Mater. Interfaces 10 (2018) 31648–31654, https://doi.org/10.1021/acsami.8b11623
[42] H. Song, L. Wei, C. Chen, C. Wen, F. Han, Photocatalytic production of H_2O_2 and its in situ utilization over atomic-scale Au modified MoS_2 nanosheets, J. Catal. 376 (2019) 198–208, https://doi.org/10.1016/j.jcat.2019.06.015
[43] M. Joy, A.P. Mohamed, K.G.K. Warrier, U.S. Hareesh, Visible-light-driven photocatalytic properties of binary MoS_2/ZnS heterostructured nanojunctions synthesized via one-step hydrothermal route, N. J. Chem. 41 (2017) 3432–3442, https://doi.org/10.1039/c6nj03727e
[44] S. Mouri, Y. Miyauchi, K. Matsuda, Tunable photoluminescence of monolayer MoS_2 via chemical doping, Nano Lett. 13 (2013) 5944–5948, https://doi.org/10.1021/nl403036h
[45] W. Zhao, Y. Liu, Z. Wei, S. Yang, H. He, C. Sun, Fabrication of a novel p-n heterojunction photocatalyst n-$BiVO_4$@p-MoS_2 with core-shell structure and its excellent visible-light photocatalytic reduction and oxidation activities, Appl. Catal. B Environ. 185 (2016) 242–252, https://doi.org/10.1016/j.apcatb.2015.12.023
[46] M. Liu, M.S. Hybertsen, Q. Wu, A. Physical, Model for understanding the activation of MoS_2 basal-plane sulfur atoms for the hydrogen evolution reaction, Angew. Chem. - Int. Ed. 2020 (2020) 1–6, https://doi.org/10.1002/anie.202003091